








Article

High-Pressure X-ray Diffraction and DFT Studies on Spinel FeV_2O_4

Josu Sánchez-Martín ¹, Robin Turnbull ^{1,*} , Akun Liang ¹ , Daniel Díaz-Anichtchenko ¹ , Saqib Rahman ², Hajra Saqib ^{3,4}, Mujtaba Ikram ⁵, Catalin Popescu ⁶ , Plácida Rodríguez-Hernández ⁷, Alfonso Muñoz ⁷ , Julio Pellicer-Porres ¹  and Daniel Errandonea ¹ 

¹ Departamento de Física Aplicada-ICMUV, MALTA-Consolider Team, Universitat de València, Calle Dr. Moliner 50, 46100 Burjassot, Spain

² Hangzhou Institute for Advanced Study, School of Physics and Optoelectronics Engineering, University of Chinese Academy of Sciences, Hangzhou 310024, China

³ Center for High Pressure Science and Technology Advanced Research, Shanghai 201203, China

⁴ Govt. Graduate College Satellite Town Rawalpindi, Rawalpindi 46300, Pakistan

⁵ Department of Materials Science and Engineering, University of Science and Technology of China, 96 Jin Zhai Rd, Hefei 230026, China

⁶ CELLS-ALBA Synchrotron Light Facility, 08290 Cerdanyola del Vallès, Spain

⁷ Departamento de Física, MALTA-Consolider Team, Instituto de Materiales y Nanotecnología, Universidad de La Laguna, 38200 Santa Cruz de Tenerife, Spain

* Correspondence: robin.turnbull@uv.es

Abstract: We have studied the behaviour of the cubic spinel structure of FeV_2O_4 under high-pressure by means of powder X-ray diffraction measurements and density-functional theory calculations. The sample was characterized at ambient conditions by energy-dispersive X-ray spectroscopy, Raman spectroscopy, and X-ray diffraction experiments. One of the main findings of this work is that spinel FeV_2O_4 exhibits pressure-induced chemical decomposition into V_2O_3 and FeO around 12 GPa. Upon pressure release, the pressure-induced chemical decomposition appears to be partially reversible. Additionally, in combination with density-functional theory calculations, we have calculated the pressure dependence of the unit-cell volumes of both the spinel and orthorhombic FeV_2O_4 crystal structures, whose bulk moduli are $B_0 = 123(9)$ and $154(2)$ GPa, respectively, finding the spinel FeV_2O_4 to exhibit the lowest bulk modulus amongst the spinel oxides. From experimental results, the same information is herein obtained for the cubic structure only. The Raman modes and elastic constants of spinel FeV_2O_4 have also been obtained at ambient conditions.

Keywords: spinel; vanadate; high pressure; X-ray diffraction; equation of state; bulk modulus; compressibility; decomposition; Raman; DFT



Citation: Sánchez-Martín, J.; Turnbull, R.; Liang, A.; Díaz-Anichtchenko, D.; Rahman, S.; Saqib, H.; Ikram, M.; Popescu, C.; Rodríguez-Hernández, P.; Muñoz, A.; et al. High-Pressure X-ray Diffraction and DFT Studies on Spinel FeV_2O_4 . *Crystals* **2023**, *13*, 53. <https://doi.org/10.3390/cryst13010053>

Academic Editor: Sergio Brutti

Received: 14 December 2022

Revised: 21 December 2022

Accepted: 22 December 2022

Published: 28 December 2022



Copyright: © 2022 by the authors. Licensee MDPI, Basel, Switzerland. This article is an open access article distributed under the terms and conditions of the Creative Commons Attribution (CC BY) license (<https://creativecommons.org/licenses/by/4.0/>).

1. Introduction

The structures of spinel-type materials were first studied over 100 years ago [1], and they remain relevant today [2–5]. The FeV_2O_4 mineral, also known as coulsonite or iron vanadate, which belongs to the family of cubic structured spinels, was discovered in 1937 [6] in natural magnetite-bearing rocks. However, it was not properly characterized until 1962, when isolated samples were found [7]. Its first crystal structure data came later (1969) when it was synthesized in the laboratory [8].

This particular FeV_2O_4 spinel has attracted several scientific studies since its discovery due to its tuneable physical [9,10] and chemical [11] properties, and its low temperature magnetic phases [12,13]. Its primary use is as an anode material in alternative Na-ion batteries [14]. It is also a light-absorbing material [15] employed as a photocatalyst with environmentally friendly purposes, including those in CO_2 reduction [16] or in antibacterial applications [17].

Spinel vanadates have also been studied under conditions of high-pressure (HP) and high-temperature (HT) [18–20]. First, Kismarahardja studied the dielectric and conducting properties of three spinel vanadates under a high magnetic field and HP [18]. Later, Li et al. performed density-functional theory (DFT) calculations to determine the bulk moduli of several spinel vanadates, finding the FeV_2O_4 bulk modulus to be 165(5) GPa [19]. Further on, Ishii et al. experimentally found three different post-spinel structures, in different compounds, (MgV_2O_4 , FeV_2O_4 , and MnCr_2O_4) by simultaneously applying HP and HT conditions [20]. For example, in FeV_2O_4 between 1000 and 1200 °C, they observed a decomposition into FeO and V_2O_3 at around 10 GPa followed by reconstitution into an orthorhombic FeV_2O_4 phase (space group $Cmcm$, number 63) at around 12 GPa, which was recoverable to ambient conditions. All of these previous works motivated the present investigation into the FeV_2O_4 spinel which has never before been studied under high pressure conditions at ambient temperature.

In this work, we have studied the HP structural properties of FeV_2O_4 via powder X-ray diffraction (XRD) experiments and DFT calculations up to 30 GPa. In the spinel FeV_2O_4 polycrystalline sample, detectable amounts of V_2O_3 and FeO were observed in addition to trace amounts of the orthorhombic FeV_2O_4 structure. The XRD and DFT result allowed for the determination of the room-temperature pressure–volume equation of state (EOS) of two polymorphs, namely spinel (S- FeVO) and orthorhombic (O- FeVO) types. Additionally, we have also reported the active Raman modes at ambient conditions and the elastic constants of the spinel polymorph.

2. Materials and Methods

2.1. Experimental Details

Simple solvothermal synthesis was used to obtain cubic FeV_2O_4 . 1.2120 g of iron nitrate nonahydrate ($\text{Fe}(\text{NO}_3)_3 \cdot 9\text{H}_2\text{O}$), 0.7019 g of ammonium vanadate (NH_4VO_3), and 0.2521 g of oxalic acid monohydrate were combined in 40 millilitres of methanol under vigorous stirring at room temperature. The mixture was then moved to a 100 mL Teflon-lined stainless-steel autoclave and kept in an oven at 200 °C for 24 h. The obtained powder was then repeatedly rinsed with ethanol and acetone and dried overnight. In order to ensure the synthesis of spinel compounds, the precipitates were calcined for four hours at 400–500 °C in an H_2/N_2 reducing environment [15].

Ambient conditions powder XRD measurements were carried out at *Servicio Central de Soporte a la Investigación Experimental* (SCSIE) in the University of Valencia using a Bruker D8 Advance A25 powder diffractometer with a Bragg-Brentano geometry and $\text{Cu K}\alpha_1$ radiation ($\lambda = 1.54059 \text{ \AA}$). Energy-dispersive X-ray spectroscopy (EDXS) was also performed at SCSIE in a surface electron microscope (SEM, ThermoFisher Scios 2 DualBeam) with an Oxford Ultima Max 170 detector. Raman spectra were acquired in the backscattering geometry using a 632.8 nm He-Ne laser and a Jobin-Yvon spectrometer combined with a thermoelectric-cooled multichannel CCD detector with a spectral resolution of 2 cm^{-1} . A laser power of 2 mW was used to avoid damaging the sample due to heating caused by laser absorption. HP powder XRD measurements were performed at the MSPD beamline of the ALBA synchrotron [21] using a monochromatic beam of wavelength 0.4246 \AA . The beam was focused to a $20 \text{ \mu m} \times 20 \text{ \mu m}$ full width at half maximum (FWHM) spot. A Rayonix charge-coupled device detector was used to collect XRD patterns with a sample-to-detector distance of 300 mm. The pressure-transmitting medium loaded in the DAC was a 4:1 methanol-ethanol mixture (ME). The pressure gauge used was based on the Cu equation of state (EOS) [22], with a precision of $\pm 0.1 \text{ GPa}$. The structural analysis was performed with ReX [23] and PowderCell [24].

2.2. Computer Simulations

The calculations reported here have been performed using first principles simulations in the framework of density-functional theory (DFT) using the Vienna Ab initio Simulation Package, VASP, [25–27]. The exchange-correlation energy was described using either

the generalized-gradient approximation, GGA, with the Perdew-Burke-Ernzerhof, PBE functional [28] or the local-density approximation, LDA with the Ceperley Alder prescription [29]. To improve the description of systems with strongly correlated d-electrons we performed our simulation using DFT+U methodology, in the Dudarev [30] approximation. The Hubbard correction, $U = 5.3$ eV and $U = 3.25$ eV for Fe and V, respectively, were applied to both Fe-3d and V-3d states. To consider both valence and semicore electrons we used pseudopotentials through the projector augmented wave, PAW, scheme [31,32]. To solve the Schrödinger equation, a plane wave basis with an energy cut-off of 540 eV has been used, which ensures high accuracy in the results. The integration over the Brillouin Zone (BZ) was performed with a Monkhorst-Pack [33] $10 \times 10 \times 10$ grid, which also maximizes the accuracy of the results. Our results report a set of energy, volume, and pressure data that can be fitted using an equation of state (EOS) model.

For each volume, the structural parameters of the crystalline structures and the atomic positions have been optimized. During the process of relaxation and optimization of the structure at different volumes, the requisite for relaxation was that the forces on the atoms should be less than 0.003 eV/Å, and that the stress tensor was diagonal with differences below 0.1 GPa, to ensure hydrostaticity. The mechanical and elastic properties were studied by obtaining the elastic constants with the Le Page method implemented in the VASP code [34]. The lattice-dynamics calculations have been performed using the open-source Phonopy package [35] interfaced with VASP. From our simulations, we obtain the phonon frequency and the irreducible representation of the modes at the Brillouin Zone centre.

3. Results and Discussion

3.1. Ambient Conditions Sample Characterization of Starting Material

The EDXS results (see Figure 1a) show that the molar ratio between Fe and V in the sample is 1:2, as expected from the chemical formula. The oxygen concentration cannot be quantified directly due to the characteristics of the detector window, however, the presence of oxygen can be confirmed, as seen in Figure 1a. No other chemical elements are detected from EDXS.

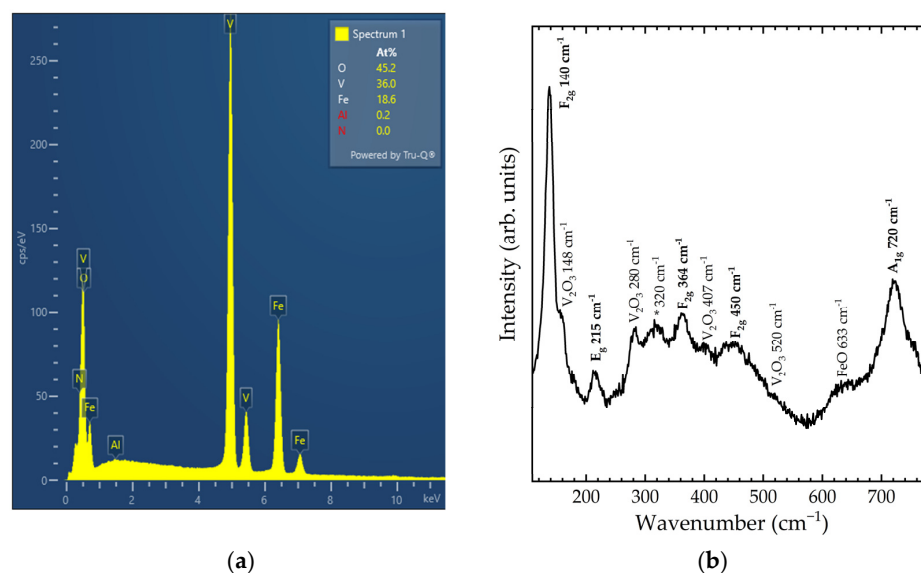


Figure 1. (a) EDXS analysis results and (b) Raman spectrum of the as-synthesised sample. Modes related to spinel FeV_2O_4 are labelled in bold.

The representative Raman spectrum in Figure 1b shows more than the expected Raman-active modes for S-FeVO. Eleven modes are observed in the spectrum, five of which are associated with V_2O_3 [36] or FeO [37], as labelled in Figure 1b. The five modes, which originate from S-FeVO, have been tentatively assigned by comparison with other spinel vanadates and with DFT calculations. The unassigned mode (marked with an asterisk in

Figure 1b) may originate from cation disorder or partial inversion, both of which are typical phenomena in spinel oxides [38,39]. The experimentally observed vibrational frequencies are compared in Table 1 with those of DFT calculations, and also with literature values for isostructural CoV_2O_4 and MnV_2O_4 [40,41]. It is found that DFT calculations overestimate the frequencies of the three low-frequency modes and underestimate the frequencies of the two high-frequency ones. The difference is more pronounced for the A_{1g} mode, which is usually assigned to an internal stretching vibration of the VO_4 tetrahedron. When compared with the literature values for other vanadates, all three vanadate compounds have a similar mode distribution, albeit with the A_{1g} mode of FeV_2O_4 at a slightly higher frequency and the low-frequency F_{2g} mode at a slightly lower frequency.

Table 1. Experimental and calculated Raman mode frequencies (cm^{-1}) of spinel FeV_2O_4 at ambient conditions compared with those of other isostructural vanadates.

Mode	FeV ₂ O ₄ (This Work)		CoV ₂ O ₄ [40]	MnV ₂ O ₄ [40,41]
	Theory (DFT)	Experiment	Experiment	Experiment
F _{2g}	190	140(2)	192	178
E _g	295	215(2)	-	-
F _{2g}	404	364(2)	356	348
F _{2g}	435	450(2)	480	476
A _{1g}	569	720(2)	676	656

The elastic constants of S-FeVO determined from DFT calculations are presented in Table 2. At ambient conditions, the three constants are close to the ones reported in the literature [19] and satisfy the zero-pressure Born stability criteria ($C_{11} + 2C_{12} > 0$, $C_{44} > 0$, $(C_{11} - C_{12})/2 > 0$), which is consistent with the mechanical stability of the S-FeVO crystal structure. From these constants, the elastic moduli were also obtained using the Hill approximation. The elastic moduli are also shown in Table 2. The values of the bulk and shear moduli show that in spinel FeV_2O_4 , shear deformation requires less energy than compressional deformation. The Bulk/Shear modulus ratio of 2.751 supports the observation that S-FeVO is ductile [42].

Table 2. DFT calculated elastic constants of S-FeVO.

Elastic Moduli (GPa)	Elastic Constants (GPa)			
0 GPa	0 GPa	9.7 GPa	11.1 GPa	12.5 GPa
Bulk modulus = 168.7	C_{11} = 259.9	C_{11} = 260	C_{11} = 171	C_{11} = −229
Shear modulus = 61.3	C_{12} = 123.2	C_{12} = 54	C_{12} = 444	C_{12} = 429
Young modulus = 164.1	C_{44} = 57.0	C_{44} = 49	C_{44} = 49	C_{44} = −11

The final part of this section relates to the sample characterisation via ambient conditions X-ray diffraction. The cubic structure of S-FeVO (space group $Fd-3m$, number 227) was successfully refined against the observed XRD pattern shown in Figure 2, which also showed small contributions from hexagonal V_2O_3 (space group $R-3c$, number 167) and cubic FeO (space group $Fm-3m$, number 225). Additionally, a detectable contribution from orthorhombic O-FeVO (space group $Cmcm$, number 63) reported by Ishii et al. [20] is also observed. For example, the reflections observed at 26° and 46° can only be explained with the (002) and (132) reflections of O-FeVO. We also used the HP XRD data (Figure 3) to support this phase identification. The multi-phase Rietveld refinement at ambient conditions, along with phase percentages and goodness parameters, is presented in Figure 2. In the refinement, the background was fitted with a Chebyshev polynomial function of the first kind with eight coefficients, and the overall displacement factor, B , was fixed to 0.5 \AA^2 [43]. The unit-cell parameter of the spinel phase is $8.335(8) \text{ \AA}$. Fe and V atoms are fixed by symmetry at (0,0,0) 8a Wyckoff position and (5/8,5/8,5/8) 16d Wyckoff position, respectively.

Oxygen atoms are at (u,u,u) 32e Wyckoff position, with $u = 0.386(3)$. The bond distances are $V-O = 1.993(3)$ Å and $Fe-O = 1.961(3)$ Å and the bond angles are $V-O-Fe = 121.5(4)^\circ$, $V-O-V = 95.1(3)^\circ$, $O-Fe-O = 109.4(4)^\circ$, and $O-V-O = 95.4(3)^\circ$.

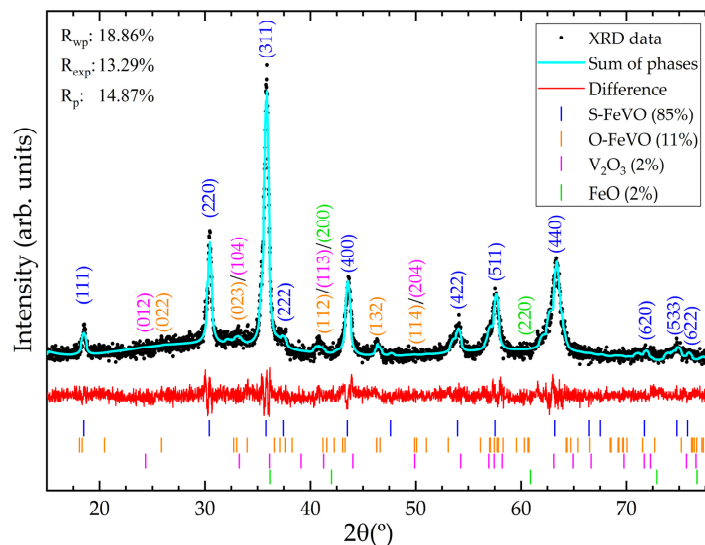


Figure 2. Multi-phase Rietveld refinement at ambient conditions of S-FeVO including the additional minor phases. Black dots are the measured pattern. The solid cyan line is the overall calculated Rietveld profile. The difference between the observed and calculated data is shown with a red line. Tick marks indicate the calculated Bragg peak positions. Relevant reflections are labelled with their corresponding Miller indices.

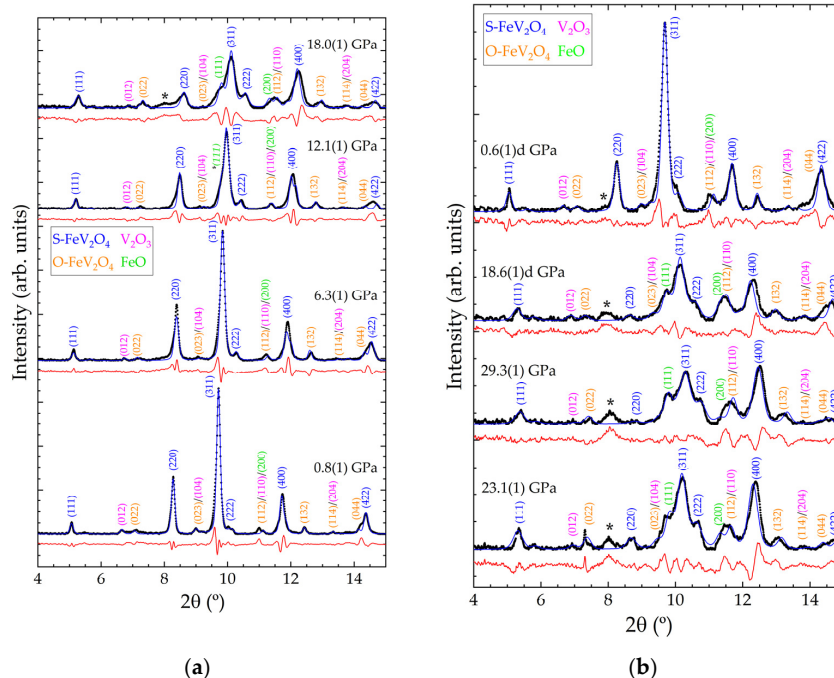


Figure 3. XRD patterns from FeV_2O_4 sample at selected pressures. (a) Increasing pressure from 0.8(1) to 18.0(1) GPa. (b) Increasing pressure from 23.1(1) GPa to the maximum pressure, 29.3(1) GPa, followed by decompression to 0.6(1) GPa. Observed data are shown with black symbols. Le Bail profiles and residuals are shown with blue and red lines, respectively. Relevant reflections are indicated with their Miller indices, with the colour of the text matching with the phases as indicated in the legend. Pressures are indicated in the figure. The letter 'd' after the labelled pressure corresponds to data acquired on sample decompression. The asterisk '*' marks the unindexed reflection which begins to emerge at 18 GPa.

3.2. High-Pressure Powder X-ray Diffraction Analysis

Figure 3 shows integrated polycrystalline XRD data acquired on compression and decompression for S-FeVO and the corresponding Rietveld profiles. Measurements were performed on various sample locations to prevent the appearance of Cu reflections in these patterns. All minor phases are observed up to the maximum pressure of 29.3(1) GPa and on recovery to ambient conditions. The highest intensity reflection in the data shown in Figure 3 originates from the (311) reflection in the S-FeVO structure. This reflection starts to develop a left shoulder contribution at 12.1(1) GPa (see the reflection marked $^{*}(111)$ in Figure 3a). As pressure further increases, this shoulder contribution gradually gains intensity when compared to the rest of the pattern. This phenomenon observed in the experimental data is consistent with the DFT calculations, which find that the S-FeVO structure becomes mechanically unstable at 11.1 GPa. In addition, above 12 GPa, the calculations predict imaginary phonons and elastic constants (see Table 2). We found that at pressures larger or equal to 11.1 GPa the calculated elastic constants violate the generalised Born criteria of stability under pressure (P) ($M_1 = (C_{11} + 2C_{12})/3 + P/3 > 0$, $M_2 = C_{44} - P > 0$, $M_3 = (C_{11} - C_{12})/2 - P > 0$) [44]. This can be seen in Figure 4 where we represent the Born criteria conditions M_i versus pressure. At 11.1 GPa, only M_2 is violated. The failure through $M_2 < 0$, called the Born instability, is characterized by symmetry breaking with a coupling of shear modes under volume conservation [45]. At 12.5 GPa, M_3 is also violated, which implies a pure shear instability. In the same pressure range, M_1 abruptly changes decreasing with pressure beyond 11.1 GPa. This behaviour implies a decrease of the bulk modulus when pressure increases, which means a decohesion of the crystal structure, supporting the notion that the crystal structure becomes destabilised at high pressures [45,46].

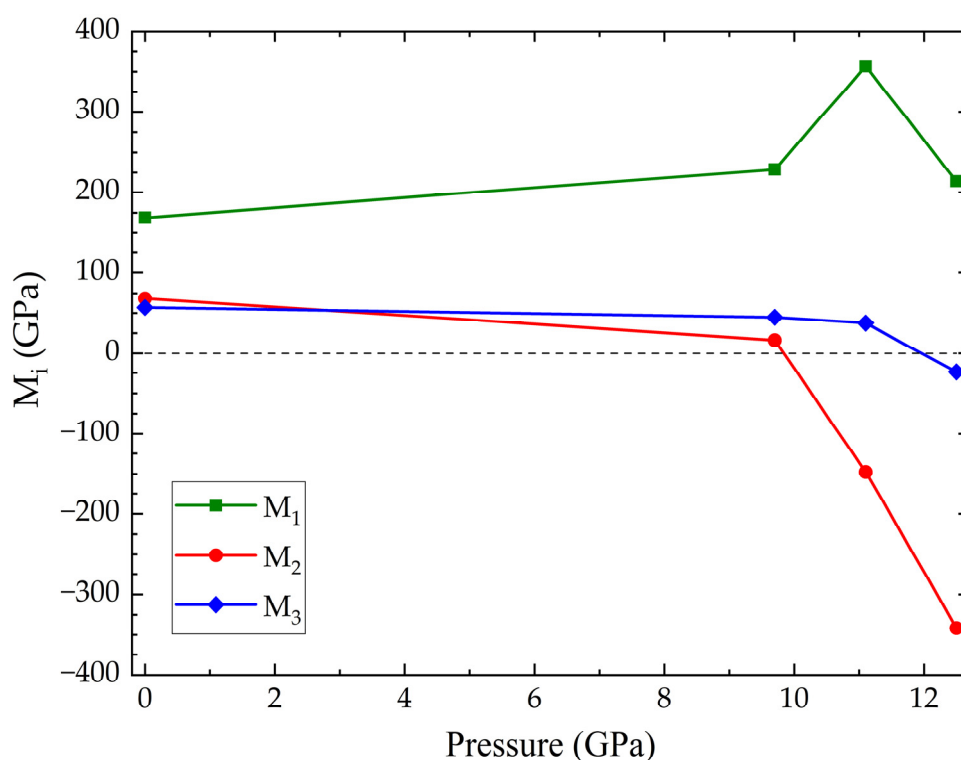


Figure 4. Generalized Born stability criteria (M_i) versus pressure for S-FeVO. In the figure M_2 and M_3 become negative at the conditions described in the text.

One possible explanation for the appearance of the peak marked as $^{*}(111)$ in Figure 3a and the broadening of peaks of cubic FeV_2O_4 could be related to a structural phase transition. The changes in the patterns are typical of phase transitions involving a symmetry decrease. We tested possible HP structures by applying group-subgroup relationships

to spinel FeV_2O_4 . We have tested the tetragonal post-spinel structure proposed by Yong et al. [47]. However, following this method we could not successfully explain the changes observed in the XRD patterns because the candidate HP structures all exhibited unit volumes larger than that of the low-pressure phase, which cannot be possible. We have also tested the known high-pressure post-spinel phases (CaFe_2O_4 -, CaMn_2O_4 -, and CaTi_2O_4 -type [48]) and found that these post-spinel structures also could not explain the changes observed in the XRD patterns. We did not consider cation inversion between Fe and V, because these elements have a similar atomic number, which does not allow us to determine the amount of element substitution from the present experiments. However, we are fully aware that cation substitution could influence the phase stability and bulk modulus [49]. A second-possible explanation for changes in XRD is pressure-induced decomposition, which is known to occur at pressures below 10 GPa in vanadates [50,51]. In our case, the reflection which appears at 12 GPa can be interpreted as an indication of pressure-induced chemical decomposition of the sample because the reflection corresponds to the (111) reflection of FeO. The reflections assigned to V_2O_3 also become more intense with increasing pressure. In the ambient pressure XRD data shown in Figure 2, the Rietveld refinement suggests that the V_2O_3 and FeO each constitute around 2% of the total sample. Therefore, by comparison with the intensity of their most recognizable reflections ((012) for V_2O_3 and (111) for FeO) with the highest one of S-FeVO, (311), it is possible to quantify the decomposition. The amounts of V_2O_3 and FeO in the sample gradually increase with compression up to 14% each, whereas S-FeVO reduces to 61%. Upon decompression, the decomposition products partially recombine into the original state, ultimately constituting only around 8% of the sample at 0.6(1) d GPa. The O-FeVO contribution remains constant throughout the experiment, indicating that it does not chemically decompose or transition to another phase in the studied pressure range. The phenomenon of reversal of the pressure-induced chemical decomposition has previously been observed in other systems, including vanadates [51,52].

At 18.0(1) GPa, a new reflection emerges around 8° which shifts very little in 2θ up to the maximum pressure studied, 29.3(1) GPa, and remains in the pattern even upon recovery to ambient pressure. This suggests that an irreversible phase transition might have occurred in one of the sample phases (see asterisks in Figure 3). Attempts were made to index this reflection using a known high pressure monoclinic structure of V_2O_3 [53], since this is the only compound in our sample known to undergo a phase transition in this pressure range. However, this was not possible, and regrettably, the peak remains to be indexed.

3.3. Unit-Cell Volume and Equation of State (EOS) Parameters

The pressure dependence of the unit-cell volume of the S-FeVO, determined experimentally and via DFT calculations, is presented in Figure 5. Figure 5 also includes the DFT results for the O-FeVO polymorph. According to DFT simulations, the unit-cell parameters of the orthorhombic structure at ambient conditions are $(a, b, c) = (2.9675, 9.8332, 10.0068)$ Å for GGA+U and $(2.8836, 9.5703, 9.7654)$ Å for the LDA+U method. The experimental determination of the pressure evolution of the O-FeV₂O₄ unit-cell volume was not possible due to the low signal intensity. Third-order Birch-Murnaghan EOS [54] was fitted to the experimental and calculated data using the EosFit7 software [55]. We also calculated the Eulerian strain vs. normalized pressure in order to choose the correct order of the EOS.

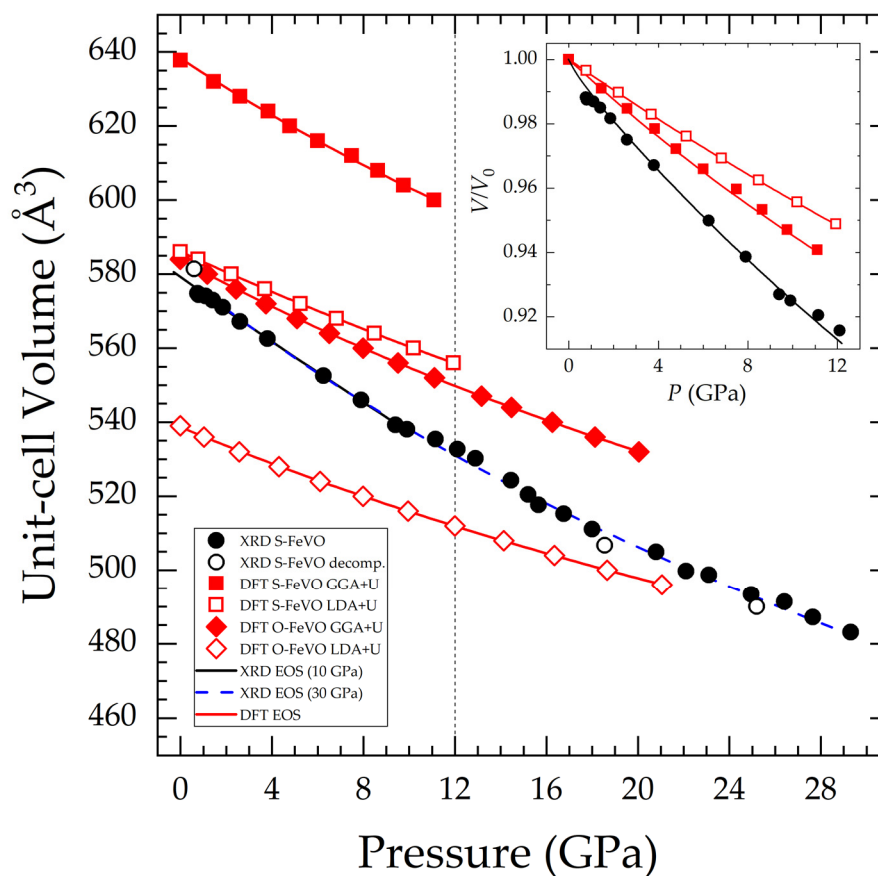


Figure 5. FeV_2O_4 unit-cell volume as a function of pressure. Black filled circles correspond to experimental S-FeVO on compression and open circles to S-FeVO on decompression data. Red squares represent DFT S-FeVO (filled for GGA+U and empty for LDA+U). Red diamonds represent DFT O-FeVO (with the displayed volume doubled in order to correspond to the same number of formula units). Lines correspond to third order Birch-Murnaghan EOS. Two EOS are fitted to the experimental S-FeVO data, one up to 10 GPa and one up to the maximum pressure. The vertical dashed line at 12 GPa corresponds to the critical pressure for the onset of pressure-induced chemical decomposition. The normalized volume for S-FeVO data is shown in the inset.

The relevant EOS parameters corresponding to the EOS shown in Figure 5 are presented in Table 3. Even though we separated the EOS analysis into quasi and non-hydrostatic regions (ME mixture behaves hydrostatically up to 10 GPa [56]), the experimental results are quite similar. When comparing the experimental results with those from DFT calculations, we found that the LDA calculations describe more accurately than GGA calculations the unit-cell volume of spinel-type FeV_2O_4 at zero pressure. However, the GGA approximation gives a description of the compressibility of spinel-type FeV_2O_4 more similar to experiments than LDA (see for instance the inset of Figure 5). This is not surprising since the LDA description tends to over-bind atoms so that the bulk modulus is overestimated. GGA corrects this fact but may under-bind instead, leading to longer bond lengths and consequently a larger unit-cell volume. The observed difference between experiments and calculations is within the typical discrepancies [57]. This difference could also originate from non-hydrostatic stresses in the sample environment [58]. It is also possible that the presence of minority phases and impurities would affect the compressibility of S-FeVO as observed in other compounds [59]. It is also possible, that the actual magnetic structure may be more complicated than what we have assumed in the theoretical calculations [60]. Such systematic discrepancy deserves a systematic discussion, which is beyond the scope of this work. The structure of O-FeVO is less compressible than that

of S-FeVO, and it has a smaller volume than S-FeVO. These facts agree with not seeing any significant change in the amount of O-FeVO during the HP XRD experiment and its non-reversible behaviour, which was reported in the literature [20]. S-FeVO exhibits the lowest bulk modulus among the spinel oxides [19], whose previously published literature values ranged from 165 to 204 GPa. We have used the DFT results on O-FeVO and PAS-Cal [61] for calculating its anisotropic axial compressibilities. At 6.5 GPa, they result as $(\kappa_a, \kappa_b, \kappa_c) = (1.767(16), 1.545(11), 1.556(9)) \times 10^{-3} \text{ GPa}^{-1}$.

Table 3. Experimental and calculated EOS Parameters for FeV_2O_4 . Ambient pressure unit-cell volume, V_0 , bulk modulus, B_0 , and its first pressure derivative, B_0' .

Source	$V_0(\text{\AA}^3)$	$B_0(\text{GPa})$	B_0'
S-FeVO up to 9.9(1) GPa	579.0(6)	123(9)	3.2(15)
	579.2(4)	118.1(17)	4(fixed)
S-FeVO up to 29.3(1) GPa	581.7(12)	122(6)	2.8(4)
	584.1(11)	106(2)	4(fixed)
S-FeVO DFT calculations GGA+U	638.3(3)	154(2)	4.99(18)
	637.2(3)	166.5(10)	4(fixed)
S-FeVO DFT calculations LDA+U	586.10(5)	206.4(15)	3.5(3)
	586.16(4)	203.6(5)	4(fixed)
O-FeVO DFT calculations GGA+U	291.95(14)	173.3(4)	4.66(5)
	291.82(4)	179.1(5)	4(fixed)
O-FeVO DFT calculations LDA+U	269.40(5)	211(3)	5.2(6)
	269.26(7)	214.1(18)	4(fixed)

4. Conclusions

HP angle dispersive powder XRD experiments and DFT calculations were performed on FeV_2O_4 up to 29.3(1) GPa. A series of ambient pressure experiments (EDXS, Raman, and XRD) demonstrated the co-existence of spinel FeV_2O_4 (85%), orthorhombic FeV_2O_4 (11%), V_2O_3 (2%), and FeO (2%). One of the main findings of this work is that upon compression to 12.1(1) GPa, the S-FeVO structure starts to chemically decompose into V_2O_3 and FeO, with the compounds both comprising around 14% of the sample at 29.3(1) GPa. This observation is supported by DFT calculations which predict the S-FeVO structure to become unstable around 12 GPa. Upon pressure release, the chemical decomposition appears to be partially reversible. The pressure dependence of the unit-cell volume and the equations of state of S-FeVO and O-FeVO are reported for DFT calculations, and a comparison is made with the experimental values for S-FeVO. The spinel and orthorhombic FeV_2O_4 bulk moduli are determined to be $B_0 = 123(9)$ and $154(2)$ GPa, respectively, finding the spinel FeV_2O_4 to exhibit the lowest bulk modulus amongst the spinel oxides [19], whose previously published literature values ranged from 165 to 204 GPa. The Raman active modes of S-FeVO were also calculated to support the findings of XRD measurements. The results obtained could also have meteoritical and petrological implications [62].

Author Contributions: X-ray diffraction measurements, J.S.-M., R.T., A.L., D.D.-A., C.P. and D.E.; Raman experiments: J.S.-M. and J.P.-P.; sample synthesis, S.R., H.S. and M.I.; DFT calculations, P.R.-H. and A.M.; formal analysis and writing, J.S.-M., R.T. and D.E.; supervision, and project administration, D.E. All authors have read and agreed to the published version of the manuscript.

Funding: This research was funded by the Spanish Research Agency (AEI) and the Spanish Ministry of Science and Investigation (MCIN) under grant PID2019-106383GB-41/43 (DOI: 10.13039/501100011033). This work was also supported by the Generalitat Valenciana under Grant No. PROMETEO CIPROM/2021/075-GREENMAT and MFA/2022/007. J.S.-M. acknowledges the Spanish Ministry of Science, Innovation, and Universities for the PRE2020-092198 fellowship. R.T. acknowledges funding from the Generalitat Valenciana through the APOSTD postdoctoral Fellowship No. CIAPOS/2021/20.

Data Availability Statement: The raw data required to reproduce the above findings are available from the authors upon a reasonable request.

Acknowledgments: The authors thank ALBA synchrotron for providing beam time for the HP XRD experiments (Proposal 2021085226). We also thank Saïd Agouram for his help in the EDXS analysis.

Conflicts of Interest: The authors declare no conflict of interest.

References

1. Bragg, W.H. XXX. The structure of the spinel group of crystals. *Philos. Mag.* **1915**, *6*, 305–315. [\[CrossRef\]](#)
2. Arita, R.; Held, K.; Lukoyanov, A.V.; Anisimov, V.I. Doped Mott Insulator as the Origin of Heavy-Fermion Behavior in LiV_2O_4 . *Phys. Rev. Lett.* **2007**, *98*, 166402. [\[CrossRef\]](#) [\[PubMed\]](#)
3. Biagioni, C.; Pasero, M. The systematics of the spinel-type minerals: An overview. *Am. Miner.* **2014**, *99*, 1254–1264. [\[CrossRef\]](#)
4. Krishna, J.; Singh, N.; Shallcross, S.; Dewhurst, J.K.; Gross, E.K.U.; Maitra, T.; Sharma, S. Complete description of the magnetic ground state in spinel vanadates. *Phys. Rev. B* **2019**, *100*, 081102. [\[CrossRef\]](#)
5. Tsurkan, V.; von Nidda, H.-A.K.; Deisenhofer, J.; Lunkenheimer, P.; Loidl, A. On the complexity of spinels: Magnetic, electronic, and polar ground states. *Phys. Rep.* **2021**, *926*, 1–86. [\[CrossRef\]](#)
6. Dunn, J. A The mineral deposits of eastern Singhbhum and surrounding areas. *Mem. Geol. Surv. India* **1937**, *69*, 21.
7. Radtke, A.S. Coulsonite, FeV_2O_4 , a spinel-type mineral from Lovelock, Nevada. *Am. Miner.* **1962**, *47*, 1284–1291.
8. Reuter, B.; Riedel, E.; Hug, P.; Arndt, D.; Geisler, U.; Behnke, J. Zur kristallchemie der vanadin(III)-spinnelle. *Z. Anorg. Allg. Chem.* **1969**, *369*, 306–312. [\[CrossRef\]](#)
9. Siratori, K. Effect of the Crystal Deformation on the Lattice Vibration of Oxide Spinel. *JPSJ* **1967**, *23*, 5. [\[CrossRef\]](#)
10. Shahi, P.; Singh, R.; Kumar, S.; Dubey, D.K.; Singh, D.N.; Tiwari, A.; Tripathi, A.; Ghosh, A.K.; Chatterjee, S. Effect of Li doping on magnetic and transport properties of CoV_2O_4 and FeV_2O_4 . *arXiv* **2015**, arXiv:1411.2415.
11. Van Vuuren, C.P.J.; Stander, P.P. The oxidation kinetics of FeV_2O_4 in the range 200–580 °C. *Thermochim. Acta* **1995**, *254*, 227–233. [\[CrossRef\]](#)
12. Gupta, M.P.; Mathur, H.B. The cation distribution in the ferrite FeV_2O_4 : Mossbauer and X-ray diffraction studies. *J. Phys. C Solid State Phys.* **1975**, *8*, 370. [\[CrossRef\]](#)
13. Roulland, F.; Roseau, G.; Pena-Corredor, A.; Wendling, L.; Krieger, G.; Lefevre, C.; Trassin, M.; Pourroy, G.; Viart, N. Promoting the magnetic exchanges in PLD deposited strained films of FeV_2O_4 thin films. *Mater. Chem. Phys.* **2022**, *276*, 125360. [\[CrossRef\]](#)
14. Maggay, I.V.B.; De Juan, L.M.Z.; Lu, J.S.; Nguyen, M.T.; Yonezawa, T.; Chan, T.S.; Liu, W.R. Electrochemical properties of novel FeV_2O_4 as an anode for Na-ion batteries. *Sci. Rep.* **2018**, *8*, 8839. [\[CrossRef\]](#)
15. Janani, B.; Swetha, S.; Syed, A.; Elgorban, A.M.; Zaghloul, N.S.S.; Thomas, A.M.; Raju, L.L.; Khan, S.S. Spinel FeV_2O_4 coupling on nanocube-like Bi_2O_3 for high performance white light photocatalysis and antibacterial applications. *J. Alloys Compd.* **2021**, *887*, 161432. [\[CrossRef\]](#)
16. Zhao, X.; Han, D.; Dai, M.; Fan, Y.; Wang, Z.; Han, D.; Niu, L. Direct Z-scheme $\text{FeV}_2\text{O}_4/\text{g-C}_3\text{N}_4$ binary catalyst for highly selective reduction of carbon dioxide. *J. Chem. Eng.* **2022**, *436*, 132051. [\[CrossRef\]](#)
17. Chinnathambi, A. Synthesis and characterization of spinel FeV_2O_4 coupled ZnO nanoplates for boosted white light photocatalysis and antibacterial applications. *J. Alloys Compd.* **2022**, *890*, 161742. [\[CrossRef\]](#)
18. Kismarahardja, A.W. *Dielectric and Conducting Properties of the Spinel Structures FeV_2O_4 , MnV_2O_4 and CoV_2O_4 in High Magnetic Field and under Very High Pressure*; FSU: Tallahassee, FL, USA, 2010.
19. Li, Z.Y.; Li, X.; Cheng, J.G.; Marshall, L.G.; Li, X.Y.A.; dos Santos, M.; Yang, W.G.; Wu, J.J.; Lin, J.F.; Henkelman, G.; et al. Anomalous bulk modulus in vanadate spinels. *Phys. Rev. B* **2016**, *94*, 165159. [\[CrossRef\]](#)
20. Ishii, T.; Sakai, T.; Kojitani, H.; Mori, D.; Inaguma, Y.; Matsushita, Y.; Yamaura, K.; Akagoi, M. High-Pressure Phase Relations and Crystal Structures of Postspinel Phases in MgV_2O_4 , FeV_2O_4 , and MnCr_2O_4 : Crystal Chemistry of AB_2O_4 Postspinel Compounds. *Inorg. Chem.* **2018**, *57*, 6648–6657. [\[CrossRef\]](#)
21. Fauth, F.; Peral, I.; Popescu, C.; Knapp, M. The new Material Science Powder Diffraction beamline at Alba synchrotron. *Powder Diffr.* **2013**, *28*, S360–S370. [\[CrossRef\]](#)
22. Dewaele, A.; Loubreyre, P.; Mezouar, M. Equations of state of six metals above 94 GPa. *Phys. Rev. B* **2004**, *70*, 094112. [\[CrossRef\]](#)
23. Bortolotti, M.; Lutterotti, L.; Lonardelli, I. ReX: A computer program for structural analysis using powder diffraction data. *J. Appl. Cryst.* **2009**, *42*, 538–539. [\[CrossRef\]](#)
24. Kraus, W.; Nolze, G. POWDER CELL—A program for the representation and manipulation of crystal structures and calculation of the resulting X-ray powder patterns. *J. Appl. Cryst.* **1996**, *29*, 301–303. [\[CrossRef\]](#)
25. Kresse, G.; Hafner, J. Ab Initio Molecular Dynamics for Liquid Metals. *Phys. Rev. B* **1993**, *47*, 558. [\[CrossRef\]](#)
26. Kresse, G.; Furthmüller, J. Efficiency of Ab-Initio Total Energy Calculations for Metals and Semiconductors Using a Plane-Wave Basis Set. *Comput. Mater. Sci.* **1996**, *6*, 15–50. [\[CrossRef\]](#)
27. Kresse, G.; Furthmüller, J. Efficient Iterative Schemes for Ab Initio Total-Energy Calculations Using a Plane-Wave Basis Set. *Phys. Rev. B* **1996**, *54*, 11169. [\[CrossRef\]](#)

28. Perdew, J.P.; Burke, K.; Ernzerhof, M. Generalized Gradient Approximation Made simple. *Phys. Rev. Lett.* **1997**, *77*, 3865. [CrossRef]
29. Alder, D.M.; Alder, B.J. Ground state of the electron gas by a stochastic method. *Phys. Rev. Lett.* **1980**, *45*, 566. [CrossRef]
30. Dudarev, S.L.; Botton, G.A.; Savrasov, S.Y.; Humphreys, C.J.; Sutton, A.P. Electron-energy-loss spectra and the structural stability of nickel oxide: An LSDA+U study. *Phys. Rev. B* **1998**, *57*, 1505. [CrossRef]
31. Blöchl, P.E. Projector Augmented-Wave Method. *Phys. Rev. B* **1994**, *50*, 17953. [CrossRef]
32. Kresse, I.G.; Joubert, D. From ultrasoft pseudopotentials to the projector augmented-wave method. *Phys. Rev. B* **1999**, *59*, 1758. [CrossRef]
33. Monkhorst, H.J.; Pack, J.D. Special Points for Brillouin-Zone Integration. *Phys. Rev. B* **1976**, *13*, 5188. [CrossRef]
34. Le Page, Y.; Saxe, P. Symmetry-General Least-Squares Extraction of Elastic Data for Strained Materials from Ab Initio Calculations of Stress. *Phys. Rev. B* **2002**, *65*, 104104. [CrossRef]
35. Togo, A.; Tanaka, I. First principles phonon calculations in materials science. *Scr. Mater.* **2015**, *108*, 1–5. [CrossRef]
36. Shvets, P.; Dikaya, O.; Maksimova, K.; Goikhman, A. A review of Raman spectroscopy of vanadium oxides. *J. Raman Spectrosc.* **2019**, *50*, 1226–1244. [CrossRef]
37. De Faria, D.L.A.; Silva, S.V.; de Oliveira, M.T. Raman microspectroscopy of some iron oxides and oxyhydroxides. *J. Raman Spectrosc.* **1998**, *28*, 873–878. [CrossRef]
38. Saccone, F.D.; Ferrari, S.; Errandonea, D.; Grinblat, F.; Bilovol, V.; Agouram, S. Cobalt ferrite nanoparticles under high pressure. *J. Appl. Phys.* **2015**, *118*, 075903. [CrossRef]
39. D'Ippolito, V.; Andreozzi, G.B.; Bersani, D.; Lottici, P.P. Raman fingerprint of chromate, aluminate and ferrite spinels. *J. Raman Spectrosc.* **2015**, *46*, 1255–1264. [CrossRef]
40. Byrum, T.M. Raman Scattering Studies of Spinel CoV₂O₄ and MnV₂O₄. Ph.D. Dissertation, University of Illinois, Urbana-Champaign, IL, USA, 2016. Available online: <https://hdl.handle.net/2142/92693> (accessed on 10 November 2014).
41. Singha, M.; Paul, B.; Gupta, R. Low temperature phonon studies and evidence of structure–spin correlations in MnV₂O₄. *J. Appl. Phys.* **2020**, *127*, 145901. [CrossRef]
42. Errandonea, D.; Ferrer-Roca, C.; Martínez-García, D.; Segura, A.; Muñoz, A.; Rodríguez-Hernández, P.; López-Solano, J.; Alconchel, S.; Sapiña, F. High-pressure X-ray diffraction and ab initio study of Ni₂Mo₃N, Pd₂Mo₃N, Pt₂Mo₃N, Co₃Mo₃N, and Fe₃Mo₃N: Two families of ultra-incompressible bimetallic interstitial nitrides. *Phys. Rev. B* **2010**, *82*, 174105. [CrossRef]
43. Errandonea, D.; Kumar, R.S.; Gomis, O.; Manjón, F.J.; Ursaki, V.V.; Tiginyanu, I.M. X-ray diffraction study on pressure-induced phase transformations and the equation of state of ZnGa₂Te₄. *J. Appl. Phys.* **2013**, *114*, 233507. [CrossRef]
44. Wang, J.; Yip, S. Crystal instabilities at finite strain. *Phys. Rev. Lett.* **1993**, *71*, 4182. [CrossRef] [PubMed]
45. Grimvall, G.; Magyari-Köpe, B.; Ozoliņš, V.; Persson, K.A. Lattice instabilities in metallic elements. *Rev. Mod. Phys.* **2012**, *84*, 945. [CrossRef]
46. Singh, J.; Sahoo, S.S.; Venkatakrishnan, K.; Vaitheeswaran, G.; Errandonea, D. High-pressure study of the aurophilic topological Dirac material AuI. *J. Alloys Compd.* **2022**, *928*, 167178. [CrossRef]
47. Yong, W.; Botis, S.; Shieh, S.R.; Shi, W.; Withers, A.C. Pressure-induced phase transition study of magnesiochromite (MgCr₂O₄) by Raman spectroscopy and X-ray diffraction. *Phys. Earth Planet. Int.* **2012**, *196*, 75–82. [CrossRef]
48. Errandonea, D.; Kumar, R.S.; Manjón, F.J.; Ursaki, V.V.; Rusu, E.V. Post-spinel transformations and equation of state in ZnGa₂O₄: Determination at high pressure by in situ X-ray diffraction. *Phys. Rev. B* **2009**, *79*, 024103. [CrossRef]
49. Hazen, R.M.; Yang, H. Effects of cation substitution and order-disorder on P-V-T equations of state of cubic spinels. *Am. Miner.* **2015**, *84*, 1956–1960. [CrossRef]
50. Díaz-Anichtchenko, D.; Turnbull, R.; Bandiello, E.; Anzellini, S.; Achary, S.N.; Errandonea, D. Pressure-induced chemical decomposition of copper orthovanadate (α -Cu₃V₂O₈). *J. Mater. Chem. C* **2021**, *9*, 13402–13409. [CrossRef]
51. Sakuntala, T.; Arora, A.K.; Sivasubramanian, V.; Rao, R.; Kalavathi, S.; Deb, S.K. Pressure-induced amorphization and decomposition in ZrV₂O₇: A Raman spectroscopic study. *Phys. Rev. B* **2007**, *75*, 174119. [CrossRef]
52. Vyazovkin, S. Kinetic effects of pressure on decomposition of solids. *Int. Rev. Phys. Chem* **2020**, *39*, 35–66. [CrossRef]
53. Quian, Z.; Xiang, W.; Shan, Q. Pressure-Induced Phase Transition of V₂O₃. *Chin. Phys. Lett.* **2012**, *29*, 106101. [CrossRef]
54. Birch, F. Finite Elastic Strain of Cubic Crystals. *Phys. Rev.* **1947**, *71*, 809–824. [CrossRef]
55. Gonzalez-Platas, J.; Alvaro, M.; Nestola, F.; Angel, R. EosFit7-GUI: A New Graphical User Interface for Equation of State Calculations, Analyses and Teaching. *J. Appl. Cryst.* **2016**, *49*, 1377–1382. [CrossRef]
56. Klotz, S.; Chervin, J.-C.; Munsch, P.; Le Marchand, G. Hydrostatic Limits of 11 Pressure Transmitting Media. *J. Phys. D Appl. Phys.* **2009**, *42*, 075413. [CrossRef]
57. Janthon, P.; Luo, S.A.; Kozlov, S.M.; Viñes, F.; Limtrakul, J.; Truhlar, D.G.; Illas, F. Bulk Properties of Transition Metals: A Challenge for the Design of Universal Density Functionals. *J. Chem. Theory Comput.* **2014**, *10*, 3832–3839. [CrossRef]
58. Errandonea, D.; Meng, Y.; Somayazulu, M.; Häusermann, D. Pressure-Induced $\alpha \rightarrow \omega$ Transition in Titanium Metal: A Systematic Study of the Effects of Uniaxial Stress. *Phys. B* **2005**, *355*, 116–125. [CrossRef]
59. Pereira, A.L.J.; Errandonea, D.; Beltrán, A.; Gracia, L.; Gomis, O.; Sans, J.A.; García-Domene, B.; Miquel-Veyrat, A.; Manjón, F.J.; Muñoz, A. Structural study of α -Bi₂O₃ under pressure. *J. Phys. Condens. Matter* **2013**, *25*, 475402. [CrossRef]
60. Rajeswaran, B.; Khomskii, D.I.; Zvezdin, A.K.; Rao, C.N.R.; Sundaseran, A. Field-induced polar order at the Néel temperature of chromium in rare-earth orthochromites: Interplay of rare-earth and Cr magnetism. *Phys. Rev. B* **2012**, *86*, 214409. [CrossRef]

61. Cliffe, M.J.; Goodwin, A.L. PASCAL: A Principal Axis Strain Calculator for Thermal Expansion and Compressibility Determination. *J. Appl. Cryst.* **2012**, *45*, 1321–1329. [[CrossRef](#)]
62. Ishii, T.; Kojitani, H.; Tsukamoto, S.; Fujino, K.; Mori, D.; Inaguma, Y.; Tsujino, N.; Yoshino, T.; Yamazaki, D.; Higo, Y.; et al. High-pressure phase transitions in FeCr_2O_4 and structure analysis of new post-spinel FeCr_2O_4 and $\text{Fe}_2\text{Cr}_2\text{O}_5$ phases with meteoritical and petrological implications. *Am. Miner.* **2014**, *99*, 1788–1797. [[CrossRef](#)]

Disclaimer/Publisher's Note: The statements, opinions and data contained in all publications are solely those of the individual author(s) and contributor(s) and not of MDPI and/or the editor(s). MDPI and/or the editor(s) disclaim responsibility for any injury to people or property resulting from any ideas, methods, instructions or products referred to in the content.